Diffraction efficiency of 200-nm-period critical-angle transmission gratings in the soft x-ray and extreme ultraviolet wavelength bands

Ralf K. Heilmann,[1,]* Minseung Ahn,[1] Alex Bruccoleri,[1] Chih-Hao Chang,[1]
Eric M. Gullikson,[2] Pran Mukherjee,[1] and Mark L. Schattenburg[1]

[1]Space Nanotechnology Laboratory, MIT Kavli Institute for Astrophysics and Space Research, Massachusetts Institute of Technology, 77 Massachusetts Avenue, Cambridge, Massachusetts 02139, USA

[2]Center for X-Ray Optics (CXRO), Lawrence Berkeley National Laboratory, Berkeley, California 94720, USA

*Corresponding author: ralf@space.mit.edu

Received 22 December 2010; accepted 18 January 2011;
posted 24 January 2011 (Doc. ID 140023); published 25 March 2011

We report on measurements of the diffraction efficiency of 200-nm-period freestanding blazed transmission gratings for wavelengths in the 0.96 to 19.4 nm range. These critical-angle transmission (CAT) gratings achieve highly efficient blazing over a broad band via total external reflection off the sidewalls of smooth, tens of nanometer thin ultrahigh aspect-ratio silicon grating bars and thus combine the advantages of blazed x-ray reflection gratings with those of more conventional x-ray transmission gratings. Prototype gratings with maximum depths of 3.2 and 6 μm were investigated at two different blaze angles. In these initial CAT gratings the grating bars are monolithically connected to a cross support mesh that only leaves less than half of the grating area unobstructed. Because of our initial fabrication approach, the support mesh bars feature a strongly trapezoidal cross section that leads to varying CAT grating depths and partial absorption of diffracted orders. While theory predicts broadband absolute diffraction efficiencies as high as 60% for ideal CAT gratings without a support mesh, experimental results show efficiencies in the range of ~50–100% of theoretical predictions when taking the effects of the support mesh into account. Future minimization of the support mesh therefore promises broadband CAT grating absolute diffraction efficiencies of 50% or higher. © 2011 Optical Society of America

OCIS codes: 050.1950, 050.1960, 260.6048, 300.6560, 340.7480, 350.1260.

1. Introduction

It was already realized in the nineteenth century by Lord Rayleigh that it is theoretically possible to control the distribution of energy into different grating diffraction orders through variation of the grating groove shape and thereby to optimize gratings for their particular application [1]. A generation later, Wood was the first to realize such blazing in practice [2]. Since then blazed gratings have become commonplace in countless applications for reflection gratings as well as transmission gratings. In general, blazed reflection grating technology has made more progress, especially in wavelength bands where photons suffer strong absorption upon passage through transmission gratings, as is the case for much of the extreme ultraviolet and soft x-ray bands. The surface profile for reflection gratings can now be controlled down to the nanometer level, and high line densities have been demonstrated [3–7]. However, there are numerous applications where transmission gratings are preferred over reflection gratings due to their relaxed alignment and figure error tolerances, low mass, or the desire for a straight-through zero-order beam. In particular, for nanometer-wavelength photons blazed reflection gratings are most effective at small angles of grazing incidence, which leads to

0003-6935/11/101364-10$15.00/0

long and massive grating substrates with more challenging figure requirements than transmission gratings. It is for some of those reasons that a grating spectrometer containing hundreds of transmission gratings was incorporated into the Chandra X-Ray Observatory more than ten years ago [8]. Most of the transmission gratings on Chandra have gold grating bars that are supported by a thin polyimide membrane. They are predominantly phase-shifting transmission gratings designed for maximum diffraction efficiency at normal incidence in ± first order for x rays with wavelengths $\lambda \sim 0.15$ to 1.5 nm. For softer x rays, absorption from the membranes increases rapidly, and no known material can provide efficient, low-absorption phase shifting over a broad band.

We have recently introduced a highly efficient transmission grating concept that practically eliminates absorption concerns [9]. The so-called critical-angle transmission (CAT) gratings consist of thin, freestanding, ultrahigh aspect-ratio grating bars with nanometer-smooth sidewalls (see Fig. 1). The open gaps (width a) between grating bars (width b) make up about 80% of the grating period and provide an absorption-free medium for transmission. CAT gratings are inclined at an angle α relative to the incident photons that are less than the critical angle of total external reflection. Photons therefore undergo efficient grazing-incidence reflection off of the grating bar sidewalls. The grating depth is given by $d = a/\tan\alpha$, leading to a single reflection in a geometrical optics approximation. We previously fabricated a few CAT gratings from silicon-on-insulator (SOI) wafers with a period of 574 nm and a depth of 10 μm. The optimum incidence angle for the achieved geometry was $\alpha \sim 2.9$ degrees. At this angle, blazing with silicon becomes inefficient for wavelengths less than ~2 nm. We measured the diffraction efficiency over the 2 to 50 nm wavelength band and observed 70%–85% of the theoretically predicted values and blazing up to −33rd order [9]. However, such high efficiencies were not obtained everywhere on the ~16 mm^2 sample due to structural defects.

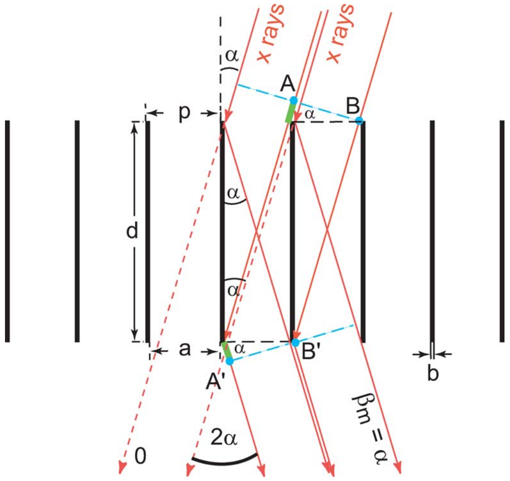

Fig. 1. (Color online) Schematic cross section through a CAT grating. The mth diffraction order occurs at an angle β_m where the path length difference between AA′ and BB′ is $m\lambda$. Shown is the case where β_m coincides with the direction of specular reflection from the grating bar sidewalls ($\beta_m = \alpha$), i.e., blazing in the mth order.

Our goal is to demonstrate high-efficiency CAT gratings that are matched to the high-resolution soft x-ray spectroscopy science case for the designated next-generation large-area x-ray telescope, the International X-Ray Observatory (IXO) [10]. This requires an incidence angle as low as 1.5° (for efficient blazing down to ~1 nm) [11–14]. Furthermore, in a broadband spectrometer application, different diffraction orders from different wavelengths will spatially overlap and a detector such as an x-ray CCD is required to “sort orders” [13]. This can be easily seen from the grating equation

$$\frac{m\lambda}{p} = \sin\alpha - \sin\beta(\lambda)_m, \tag{1}$$

where α is the angle of incidence relative to the grating normal, m is the order of diffraction ($m = 0, \pm 1, \pm 2, \ldots$), $\beta(\lambda)_m$ is the angle of diffraction for order m, and p is the grating period. For CAT gratings blazing peaks when $\beta_m = \alpha$ (specular reflection off the grating bar sidewalls). Two wavelengths λ_1 and λ_2 overlap in neighboring orders when $m\lambda_1 = (m \pm 1)\lambda_2$, and their energy difference is $\Delta E = E_2 - E_1 = \pm E_1/m$. This energy difference needs to exceed the energy resolution of the detector. For a fixed blaze angle ($\alpha + \beta(\lambda)_m = 2\alpha$), overlapping low diffraction orders differ more in energy than higher orders. Therefore, the grating period has to be small enough to provide low enough diffraction orders in the blaze direction. We have now fabricated silicon CAT gratings with a period of 200 nm [15] that peak in orders 2–10 over the 1–4 nm band that is most important for IXO. Overlapping orders differ by $\Delta E \sim 0.12$ keV, which is sufficiently large for state-of-the-art x-ray CCDs [13].

Besides having a smaller period, our new gratings were also designed to blaze optimally at smaller angles, i.e. down to shorter wavelengths. In addition, the best samples showed much improved homogeneity in terms of diffraction efficiency over their whole surface. In the samples presented here the freestanding grating bars are held in place by a support mesh of nontrivial cross section that occupies more than half of the sample area. The goal of the present work is to develop a model that takes into account the effects of the support mesh on CAT grating diffraction and to obtain a measure of CAT grating efficiencies in the absence of complications from a complex support mesh. We have begun to develop fabrication processes that are expected to lead to a simple support mesh that will take up no more than 10% of the grating area.

In the next section we shall describe the geometrical parameters of our grating samples in detail. We then describe the experimental setup and our modeling approach, which is followed by the presentation

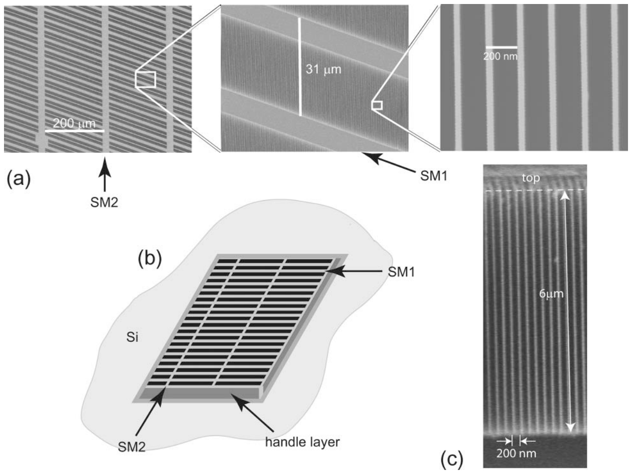

Fig. 2. (a) Top view SEM images from sample S6 at increasing magnifications from left to right, showing the support grid consisting of support mesh SM2 and support mesh SM1, with the CAT grating bars suspended from SM1 bars. Only in the leftmost image can the gap at the bottom of the SM1 mesh be seen from above. (b) Schematic of a sample, viewed from the handle layer side (not to scale). (c) SEM of a cleaved cross section parallel to mesh SM1, showing the high aspect ratio and the low duty cycle of the CAT grating bars. X rays enter from the top.

of diffraction efficiency measurements and comparison with predictions. We summarize our work at the end and provide an outlook towards ongoing and future work.

2. CAT Grating Fabrication Results

The starting points for our CAT grating fabrication are ⟨110⟩ SOI wafers where the thickness of the silicon device layer is equal to the desired grating depth. A $3 \times 3\,\mathrm{mm}^2$ hole—stopping on the thin silicon oxide layer—is etched out of the ~500-μm-thick handle layer after the patterning of both sides of the wafer (see Fig. 2). CAT grating bars and their support mesh are etched into the device layer in a single etch step. The mask pattern for the etch of the CAT grating bars has to be precisely aligned to the vertical {111} planes of the device layer to achieve maximum etch anisotropy between ⟨111⟩ and non-⟨111⟩ directions for the etch in potassium hydroxide (KOH) solution. A successful etch results in vertical grating bar sidewalls that primarily consist of atomically smooth {111} crystal lattice planes. Unfortunately, the etch also stops at inclined {111} planes that are defined by the etch mask for the support mesh. This leads to a broadening of the support mesh bars with increasing etch depth, and a reduction in open area between CAT grating bars (see Fig. 2). Details of the fabrication process have been published elsewhere [15,16].

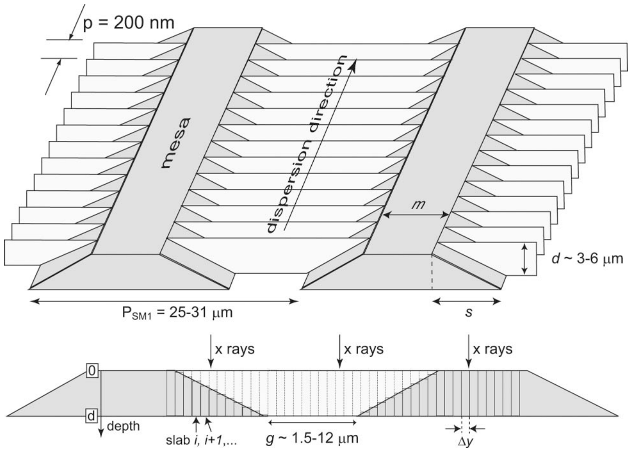

Fig. 3. Schematic of CAT grating bars with support mesh SM1 (not to scale). Top, perspective view. Support mesh bars are dark gray and CAT grating bars are light gray. Bottom, cross section through the plane of a CAT grating bar. In our model we divide the support mesh period p_{SM1} into N slabs of width Δy each. Grating depth is defined to be zero on top of the mesas and d at the bottom of the gap between support mesh bars.

In this work we focus on two samples fabricated from SOI wafers with nominal device layer thicknesses d of 4 ± 0.5 (sample S4) and $6 \pm 0.5\,\mu$m (sample S6). For both samples the grating mask was patterned via scanning beam interference lithography [17], and the support mesh via contact lithography. The support mesh forms a rhomboidal grid with a short and a long period (see Fig. 2). We assume the value p_{SM1} of the short period to be as specified in the mask design and derive the other support mesh dimensions from scanning electron micrographs (SEMs). The precise value for p_{SM1} is not overly important, as long as the other dimensions are scaled in proportion. In general, extracting accurate dimensions from standard SEMs is notoriously unreliable. Even if a single dimension in an image is known independently, scaling in the orthogonal direction can be off by several percent. Comparison of feature sizes in different parts of an image can be biased by distortions. Furthermore, noise, pixelation, and lack of contrast often make it difficult to locate feature edges accurately. The only "reliable" scale in the SEMs is the average period of the CAT gratings, which is determined with deep subnanometer accuracy in the interference lithography patterning step [17,18]. Other dimensions, therefore, have significant uncertainties, which will be reflected in the theoretical model for diffraction below.

Sample S4 was supposed to be optimized ($d = a/\tan\alpha$) for $\alpha \sim 2°$. However, during x-ray measurements it appeared that the device layer was as thin as 3–3.3 μm. SEMs of cleaved cross sections after measurements showed $d \sim 3.2\,\mu$m. The reduced thickness correspondingly led to the highest diffraction efficiencies occurring for $\alpha \sim 2.6°$.

Figure 3 defines grating depth d, widths of the sloped part (s), and the mesa (m) of the short-period support mesh bars, as well as the gap width g between supports. The long-period support mesh is parallel to the CAT grating bars and therefore has almost vertical sidewalls. It occupies a fraction F_{SM2} of the grating area. F_{open} is the fraction of the grating area that is not obscured by any part of the support mesh.

The width of the CAT grating bars is measured from both the top [device layer side, see Fig. 2(a)] and the bottom of the grating (handle layer side). Here the CAT grating period is assumed to be 200 nm and is used as a calibration scale in the SEMs. As in our previous work [9,15,19], the grating bars are slightly narrower on top (width b_{top}) than on the bottom (width b_{bot}), since the top has been exposed to the etchant much longer than the bottom. However, there are small changes in bar width from image to image (and sometimes from line to line), and top and bottom images are not necessarily from the same spot on the sample, so we can only estimate average bar widths. We estimate an average sidewall angle $\langle\epsilon\rangle$ from $\langle b_{\mathrm{top}}\rangle$, $\langle b_{\mathrm{bot}}\rangle$, and d. This might overestimate $\langle\epsilon\rangle$ slightly if there is a positive correlation between $\langle b_{\mathrm{top}}\rangle$ and $\langle b_{\mathrm{bot}}\rangle$, but this will be negligible in our analysis. For both samples, ϵ is significantly smaller than in previous work (as small as 0.02° for S4), which we believe is due to improved alignment of the grating lines to the Si {111} planes [15]. Finally, we calculate an average duty cycle $\langle \mathrm{d.c.}\rangle = \langle b\rangle/p$.

Table 1 lists the geometrical parameters for both samples and their estimated uncertainties.

3. Experimental Setup

We performed diffraction efficiency measurements in transmission at beamline 6.3.2 of the Advanced Light Source (ALS) at Lawrence Berkeley National Laboratory. The grating was mounted with its surface at the center of a goniometer. Its normal was co-aligned with the horizontal incident beam by rotating the grating around an in-plane axis parallel to the grating lines ("rocking scan") until the ±1st order diffraction peaks were of equal intensity (see, for example, Fig. 10 in [13]). We estimate this alignment procedure to be accurate or better than $\sim\pm 0.05°$. The beam was focused on a GaAsP photo diode detector, with a beam diameter of ~0.2 mm at the sample. (The convergence is small enough that the beam can still be considered collimated in the context of diffraction efficiency modeling.) We measured the transmitted intensity at a distance of 230 mm from the center of the goniometer by scanning the slit-covered detector (vertical slit width = 0.5 mm) in the vertical plane of dispersion [9].

Table 1. Geometrical Parameters for Samples S4 and S6

Sample	S4	S6
Depth d [μm]	3.2 ± 0.1	6.0 ± 0.1
Support mesh period p_{SM1} [μm]	25	31
Slope width s [μm]	5.15 ± 0.25	11.15 ± 0.25
Width g [μm]	12 ± 0.25	1.45 ± 0.15
Area fraction F_{SM2}	0.088 ± 0.004	0.106 ± 0.004
Open area fraction F_{open}	0.44 ± 0.01	0.042 ± 0.005
Linewidth b_{top} [nm]	42 ± 1	42 ± 2
Linewidth b_{bot} [nm]	44 ± 1	63 ± 3
Sidewall angle ϵ [deg]	0.02 ± 0.02	0.10 ± 0.02
Average duty cycle $\langle \mathrm{d.c.}\rangle$	0.215 ± 0.005	0.263 ± 0.013

The strongest blazing is expected close to the condition $\tan\alpha = a/d$. This can be verified by performing detector scans at a few suitable wavelengths for multiple angles close to the expected value for α. As mentioned above, for sample S4 we found d to be significantly smaller than expected, resulting in a larger optimum blaze angle of $\alpha \sim 2.6$ deg. Subsequently, we took most of our data—consisting of detector scans at a wide range of wavelengths—at $\alpha = 2.6°$ for sample S4 and $\alpha = 1.18°$ for sample S6. At each wavelength the direct beam (with the sample removed) was also measured for later normalization. The synchrotron ring current was recorded as well during all measurements and taken into account for proper normalization.

The support mesh forms a periodic grid that diffracts as well, creating satellite diffraction peaks. The supports that are parallel to the grating bars diffract in the same dispersion plane as the CAT grating. However, their period p_{SM2} is more than 3 orders of magnitude larger than p, which means that the aperture defined by the slit in front of the detector integrates over more than the first ±100 support mesh diffraction orders in that direction ($\lambda = 2$ nm). Because the long-period mesh only diffracts weakly to begin with, higher orders that fall outside of the slit aperture can safely be ignored. The short-period mesh is oriented at 70.5° relative to the CAT grating bars. Its period p_{SM1} is still more than 2 orders of magnitude larger than p, and it disperses in a direction closer to the long slit direction, where the aperture is limited by the detector diameter of 4.6 mm. Nevertheless there is a potential for missing some noticeable intensity from SM1-mesh satellite peaks. The worst case is given for long wavelengths and a strongly absorbing support mesh with a narrow gap that modulates diffraction peaks with a broad single slit diffraction envelope. We take this effect into account in our analysis.

4. Theoretical Model

A. CAT Grating Diffraction Efficiency

We have previously presented a simple model based on the Fraunhofer limit of scalar Kirchhoff diffraction theory [20] that captures much of the physics of ideal CAT gratings [9]. In this model the diffraction intensity is given by [21]

$$I(\lambda, p, \alpha, \beta, k', a, \epsilon, R) = I_{\mathrm{grat}} I_{\mathrm{slit}} R(\alpha + \epsilon, n(\lambda))(a/p)^2. \tag{2}$$

The grating interference function is given by

$$I_{\mathrm{grat}}(\lambda, p, \alpha, \beta, k') = \left|\frac{\sin k' g}{k' \sin g}\right|^2, \tag{3}$$

where $g = p(\pi/\lambda)(\sin\beta - \sin\alpha)$, and k' is the number of grating slits. Blazing and diffraction from a single slit is described by

$$I_{\mathrm{slit}}(\lambda,\alpha,\beta,a,\epsilon) = \left|\frac{\sin f}{f}\right|^2, \tag{4}$$

where $f = a(\pi/\lambda)(-\sin(\beta+\epsilon) - \sin(\alpha+\epsilon))$. Finally, R is the specular reflectivity of the grating material of index of refraction $n(\lambda)$ at grazing angle of incidence $\alpha+\epsilon$. This model gives a good qualitative description of CAT grating diffraction, and the term I_{slit} describes the blaze envelope as a function of wavelength and diffraction geometry.

A more accurate treatment of diffraction efficiency can be obtained from the rigorous coupled-wave analysis (RCWA) approach, which calculates exact solutions of Maxwell's equations for diffraction from 3D structures with 1D periodicity [22]. Generally, a grating is defined as a layer of constant thickness or depth with a periodic stepwise variation in the index of refraction in one lateral direction (see Fig. 1). We modeled sample S4 using d and $\langle \mathrm{d.c.} \rangle$ from Table 1 and $\alpha = 2.6°$. A ~1-nm-thick layer of native silicon oxide is expected on all Si surfaces, including the grating bar sidewalls. Inclusion of such an oxide layer predicts slightly higher efficiencies between $\lambda = 2.35\,\mathrm{nm}$ and $12\,\mathrm{nm}$ and slightly lower efficiencies outside of this range. However, the differences are small enough that we modeled the CAT gratings without an oxide layer. The index of refraction for silicon was taken from [23]. Because of their larger sidewall angles, we initially modeled the CAT grating bars of sample S6 as pyramids consisting of eight 750-nm-tall rectangles with widths ranging from ~62 to ~43 nm. Of course, such a multilayer model increases computation time significantly compared to a single-grating layer model. During further modeling, we found that a single 6-μm-deep grating layer model with $\alpha = 1.24°$ gave nearly identical results, and we proceeded with our analysis using the latter model.

B. Inclusion of Support Mesh

The presence of the short-period support mesh SM1 complicates diffraction modeling significantly. For wavelengths with short absorption lengths in silicon (for example $l_{\mathrm{abs}} < 100\,\mathrm{nm}$ for $4.8\,\mathrm{nm} < \lambda < 12.3\,\mathrm{nm}$), all but the thinnest parts of the support mesh are highly absorbing (see example transmission through bulk silicon in Fig. 4 for two different silicon film thicknesses). The CAT grating bars on top of the thinnest support mesh areas have almost the full depth d and therefore are expected to blaze almost as efficiently as the areas of the open gap. Consequently, in [9] we applied a simple correction factor to the theoretical CAT grating efficiency that takes absorption by the support mesh into account. However, for the shorter wavelengths (with l_{abs} exceeding $5\,\mu\mathrm{m}$) and the thinner samples employed in this work, we have to consider transmission through the thicker parts of the support mesh and the blazing effect of parts of the CAT gratings that range in depth from d all the way to zero.

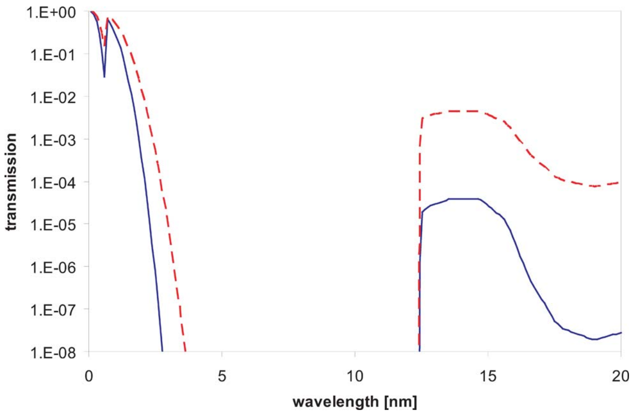

Fig. 4. (Color online) Transmission as a function of wavelength through a bulk silicon film of thickness $6\,\mu\mathrm{m}$ (solid line) and $3.2\,\mu\mathrm{m}$ (dashed line), respectively. Curves are based on data from [23].

Ideally one would model these samples as a crossed grating or grid (sometimes also called a 2D grating). However, in our case the ratio of p_{SM1} to wavelength is quite large, and algorithms require a large number of spatial harmonics to be carried for proper convergence. Even in the CAT grating direction we have $p/\lambda \sim 20$–200, and a rather large number of diffraction orders contributes significantly. Unfortunately, the memory requirement for a grid calculation roughly grows as the number of harmonics to the fourth power, compared to the number of harmonics squared for a simple grating. The number of operations required for eigenvalue and boundary value computations quickly becomes impractical, and convergence of even a single result cannot be verified in a reasonable amount of time with a fast desktop computer.

Instead, we make the following simplifying assumptions. Diffraction from SM2 is integrated over in the measurement, and the effect of this component of the support mesh can simply be modeled as transmission through a layer of silicon of thickness d that occupies a fraction F_{SM2} of the sample area. We also assume that diffraction from SM1 and from the CAT gratings can be treated independently and in sequence.

We first consider diffraction from the CAT grating bars. Those regions of the CAT grating that sit on top (in the upstream direction of the incident x rays) of the sloped SM1 sidewalls range in depth from zero to the full thickness of the device layer. We conceptually divide a single support mesh period into N vertical slabs of equal width $\Delta y = p_{\mathrm{SM1}}/N$, with each slab j consisting of a CAT grating of depth d_j on top of a layer of Si of depth $d - d_j$. The sloped sidewalls are therefore approximated as staircases (see Fig. 3). For the parts of SM1 without a CAT grating (mesa) $d_j = 0$, while the portion of the period that is unobscured by the support mesh (gap) has $d_j = d$. (We empirically determined the necessary number of slabs N per p_{SM1} by increasing N until a doubling of N changed the model predictions by a negligible amount. For most of our simulations we used

$N \sim 400$–500.) We calculate the diffracted and transmitted fields [amplitude $A_j(m)$ and phase $\Phi_j(m)$] at depth d for all CAT grating diffraction orders m for each slab j as if it were of infinite extent in the CAT grating cross-dispersion direction, using RCWA.

We then treat diffraction from the support mesh with scalar diffraction theory, assuming the support mesh to consist of an infinite number of periods. This leads to the splitting of each CAT grating diffraction peak into many satellite peaks. For each satellite diffraction order (m, k), we coherently add the transmitted fields, with added phase shifts that correspond to the additional path lengths acquired as a function of k and j. The intensity of satellite peak k of CAT grating diffraction order m is then

$$I(m,k) = \frac{1}{N^2}\left|\sum_{j=1}^{N} A_j(m) \times \exp\left[i\left(\Phi_j(m) + 2\pi k \frac{j\Delta y}{p_{\mathrm{SM1}}}\right)\right]\right|^2. \quad (5)$$

If the measurement integrates over all the satellite peaks, the measured intensity is simply given by the sum over all satellite peaks:

$$\begin{aligned} I(m) &= \sum_{k=0}^{\pm\infty} I(m,k) \\ &= \frac{1}{N^2}\sum_{k=0}^{\pm\infty}\sum_{l=1}^{N}\sum_{q=1}^{N} A_l(m)A_q^*(m) \\ &\quad \times \exp\left[i\left(\Phi_l(m) - \Phi_q(m) + 2\pi k \frac{(l-q)\Delta y}{p_{\mathrm{SM1}}}\right)\right]. \end{aligned} \quad (6)$$

In the limit of Δy going to zero ($\lim_{N\to\infty}$), the sum over k of the additional phase factor $\exp i(2\pi k(l-q)\Delta y/p_{\mathrm{SM1}})$ turns into a delta function, reducing the double sum over l and q into a single sum, and we obtain

$$I(m) = \frac{1}{N}\sum_{j=1}^{N} A_j(m)A_j^*(m) = \frac{1}{N}\sum_{j=1}^{N} |A_j(m)e^{i\Phi_j(m)}|^2. \quad (7)$$

Thus, the sum over all the satellite peak intensities is equal to the incoherent sum over all the fields at the bottom of the support mesh unit cell.

In our measurements the satellite peaks cannot be spatially resolved. We do not integrate over all satellite peaks but only over those that fall within the open part of the aperture of the slit-covered detector. Since the support mesh in our samples is at a 19.5° angle relative to the narrow slit dimension, we predict that only satellite peaks with $|k| \le k_{\max} \sim 3.3 \times 10^{-3} p_{\mathrm{SM1}}/\lambda$ contribute in the measurement of peak diffraction efficiency when performing a detector scan in the CAT grating dispersion direction. (This is the only part of our analysis where we take into account that SM1 and CAT grating bars are not orthogonal to each other.) We therefore calculate both Eq. (7) ("incoherent model") and the explicit sum over $\pm k_{\max}$ satellite peaks according to Eq. (6) ("coherent model"). For our samples and wavelengths, $k_{\max}$ ranges from as little as 4 to over 100.

5. Results

We aligned and oriented the samples relative to the synchrotron beam as described in Section 3 above. In order to check for variation in diffraction intensity across the grating surface, we scanned the samples in the plane normal to the incident beam, with the detector fixed on a blazed diffraction peak. Figure 5 shows good homogeneity across sample S4, but across sample S6 much less so. The scan in the direction normal to SM2 (solid line) also shows the effect of individual SM2 lines entering and exiting the x-ray beam. The areas of low intensity on S6 correspond to areas with physical damage that are discernible under a visible-light microscope. All further data were collected at a fixed sample position on a single spot with a high diffraction efficiency.

Figure 6 shows normalized data from detector scans at five different wavelengths for S4. Predictions from RCWA (coherent model) are included as bars. Also shown is the blaze envelope due to single slit diffraction [Eq. (4), dashed line] and the prediction from the simple model of Eq. (2) (solid line), multiplied by the average transmission per unit area through the support mesh structure. Data and theory show the expected blazing, peaked at ~2 × α, and the narrowing of the blaze envelope with decreasing wavelength. The data are close to theoretical predictions and shows efficient blazing in high orders, implying good agreement between an ideal CAT grating and the fabricated device. At shorter wavelengths the blazing effect is much reduced since α is less than the critical angle for total external reflection. At the same time the absorption length for x rays in silicon increases with decreasing wavelength, and the support mesh becomes more transmissive, resulting in

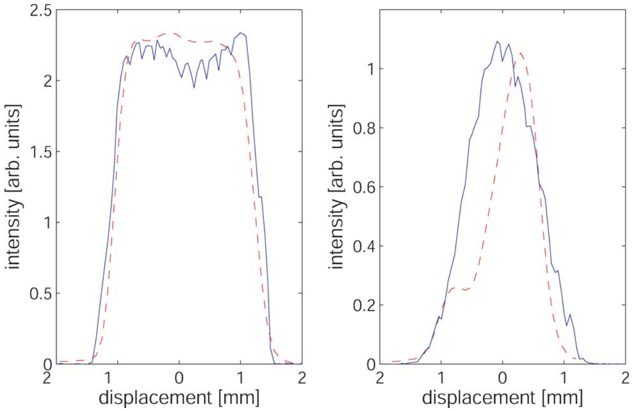

Fig. 5. (Color online) Sample scans in the plane normal to the x-ray beam. Solid lines are scans perpendicular to support mesh SM2, dashed lines parallel to SM2. (a) S4 at $\lambda = 3.5$ nm, $\alpha = 2.6°$, blazed in −5th order. (b) S6 at $\lambda = 3.0$ nm, $\alpha = 1.18°$, blazed in −3rd order.

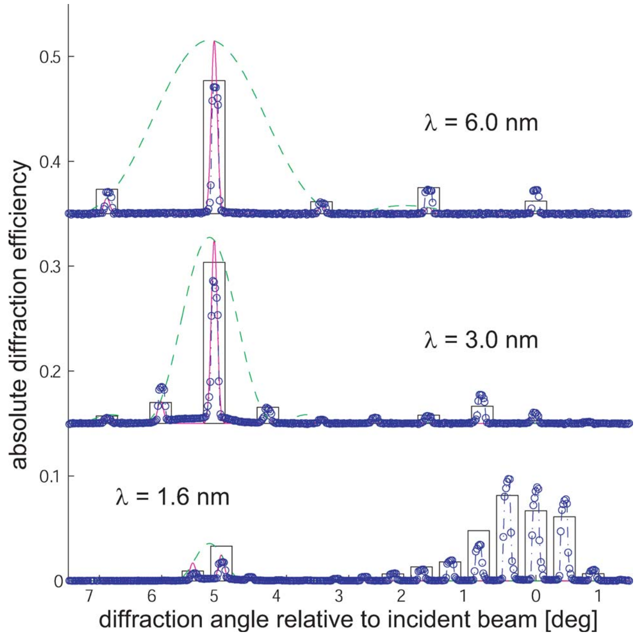

Fig. 6. (Color online) Example normalized detector scans for sample S4 at $\alpha = 2.6°$. Circles represent experimental data, the dashed line is the blaze envelope, the solid line represents the simple model, and bar heights show diffraction peak intensities predicted via RCWA (coherent model). Data and theory are shifted vertically for clarity for the different wavelengths.

stronger low-order diffraction. Of course the simple model is ignorant of the support mesh structure (apart from its absorption) and the varying CAT grating depths, and it does not predict any diffraction outside of the single slit diffraction function. There is much better agreement between RCWA and data across all wavelengths, indicating that the coherent model captures the main features of the sample.

Figure 7 shows data and theory in the same fashion for S6. Because of the small open gap and the larger depth of S6, this sample is dominated by the support mesh, and absolute diffraction efficiencies are generally lower. The smaller angle of incidence used in the measurements leads to lower diffraction orders at blaze and allows blazing towards shorter wavelengths. Even at the shortest available wavelength ($\lambda = 0.96$ nm) blazing is still visible. There is decent agreement between data and RCWA predictions. The simple model generally overestimates peak heights because it assumes ideal depths for all the CAT grating bars. This effect is especially pronounced at $\lambda = 0.96$ nm, where $l_{\text{abs}} \sim 5.5\,\mu$m and even the most "shallow" grating areas contribute to transmitted orders due to the reduced absorption from the underlying parts of the support mesh.

We extracted absolute diffraction efficiencies (ratio of measured diffraction peak intensities to direct beam intensity) for the (negative) blazed orders, as well as for zeroth and −1st orders from detector scans at a number of wavelengths. Figures 8 and 9 show these efficiencies for orders 0 through −11 as a function of wavelength for S4. Also shown is the RCWA (coherent model) prediction, using the nominal parameters from Table 1. Vertical bars at select wavelengths show how predictions from the coherent model change when we vary the parameters from Table 1 by their estimated uncertainties. When we

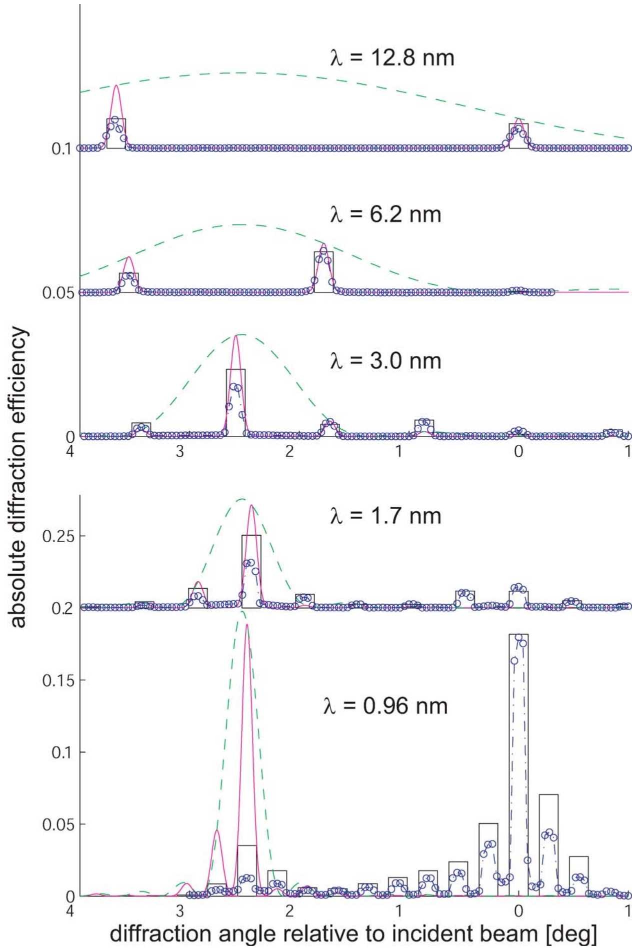

Fig. 7. (Color online) Example normalized detector scans for sample S6 at $\alpha = 1.18°$. Legend is the same as in Fig. 6.

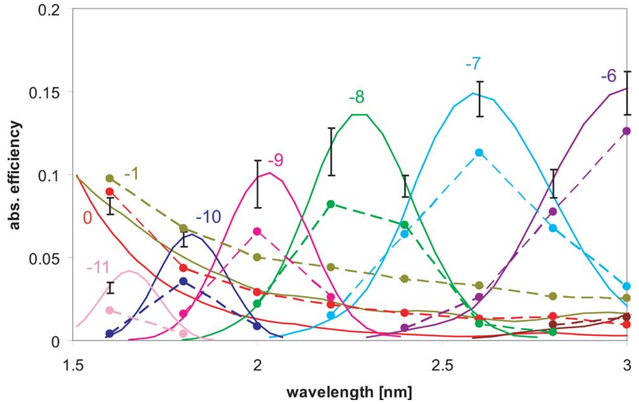

Fig. 8. (Color online) Absolute diffraction peak intensity for sample S4 as a function of wavelength for orders 0, −1, and −6 through −11. Circles are measured data, and solid lines are predictions from the coherent model. Dashed lines connect data points for a given diffraction order and serve as guides for the eye. Vertical bars show range of predicted efficiencies taking uncertainties in SEM-derived parameters into account.

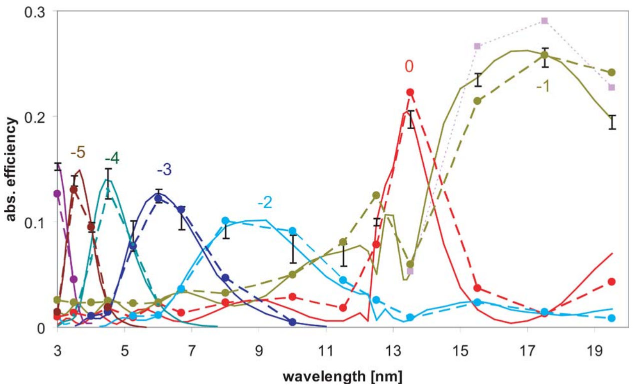

Fig. 9. (Color online) Absolute diffraction peak intensity for sample S4 as a function of wavelength for orders 0 through −5 (continued from Fig. 8 for longer wavelengths). Circles are measured data, and solid lines are predictions from the coherent model. Dashed lines connect data points for a given diffraction order and serve as guides for the eye. Vertical bars show range of predicted efficiencies taking uncertainties in SEM-derived parameters into account. The squares show predictions for −1st order from the incoherent model at four wavelengths. The jump in zeroth order efficiency around 13 nm is due to the silicon L absorption edges.

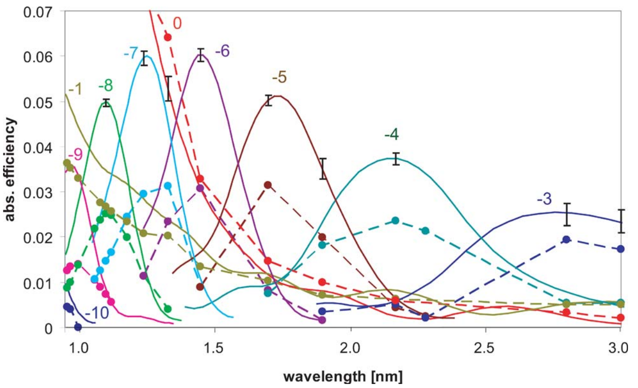

Fig. 10. (Color online) Absolute diffraction peak intensity for sample S6 as a function of wavelength for orders 0, −1, and −3 through −10. Circles are measured data, and solid lines are predictions from the coherent model. Dashed lines connect data points for a given diffraction order and serve as guides for the eye. Vertical bars show range of predicted efficiencies taking uncertainties in SEM-derived parameters into account.

look at the measured intensities close to the peaks in efficiency for each order (−6 through −11 in Fig. 8), we see that the measured intensities fall short of the predicted values by ~20%–45%. However, for the peaks that are in the wings of the blaze envelopes for each order, we find very good agreement between experiment and model. One potential reason for this could be variations in sidewall angles or bending from one CAT grating bar to the next. This is similar to a variation in incidence angle and would lead to a broadening of the blaze envelope and a concurrent reduction in its height. We also see that zeroth and −1st order transmission is higher than predicted at shorter wavelengths, which could be due to overestimation of the average sample thickness or other support mesh parameters. At the longer wavelengths in Fig. 9, we find very good agreement between measured and modeled efficiencies. There seems to be a slight "shift" in the theoretical curves towards shorter λ relative to experimental results. This could be remedied by assuming an unreasonably high value for α in the model and would lead to noticeable offsets between data and theory at shorter wavelengths. Predictions from the coherent and incoherent models follow each other very closely up to $\lambda \sim 15$ nm. At larger λ we predict some satellite peaks of significant strength to fall outside the detector slits. The difference between models can be seen from the square symbols (incoherent model) shown at four wavelengths in Fig. 9.

The results for S6 are shown in similar fashion in Figs. 10 and 11. Again we see peak efficiencies lower (~50%–75% of theory) than predicted at shorter wavelengths, and excellent agreement at larger λ.

6. Discussion

This work is a snapshot of the x-ray performance of our latest CAT grating samples fabricated via wet etch in KOH and a comparison with predictions from a physical model based on RCWA. The broadening of the support mesh with increasing etch depth leads to a reduction in CAT grating area for low-absorption throughput and complicates data analysis. Our goal here is to get feedback about the quality and performance of the CAT grating bars and, if possible, to remove the effects of the support mesh from the data. The coherent model described above allows us to do this. Based on SEM data, the model seems to provide an upper limit for the measured efficiencies without adjusting any of its parameters. The fabricated CAT grating bars achieve blazing in the range of ~50%–100% of theory. Reasons for discrepancies between model and data can be due to uncertainties in model parameters, errors and uncertainties in measurement, and structural imperfections in the samples compared to the ideal model. For example, the uncertainties in Table 1 are based on a small number of SEM images and do not take the possibility into account that grating depth or support mesh parameters could vary by more than the given uncertainties over the area sampled by the x-ray beam. In addition, several simplifying assumptions were made in the model without estimating their impact.

Sample S4 shows better agreement with model predictions, but this view might be biased somewhat due to the difference in incidence angle and the lack of data below $\lambda = 1.6$ nm. Data agree with the model very well for $\lambda > 3.5(5)$ nm for S4 (S6), but falls below predictions with decreasing λ or increasing diffraction order $|m|$ [24]. This behavior could be explained through scattering due to high spatial-frequency structural deviations from the ideal model, such as sidewall roughness and variations in duty cycle and center position for the CAT grating bars. Finite-element calculations indicate that in order to

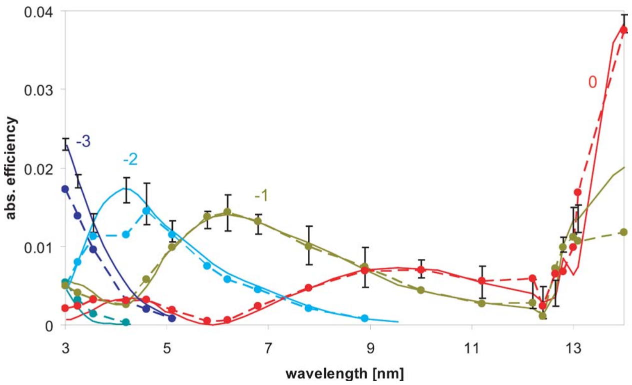

Fig. 11. (Color online) Absolute diffraction peak intensity for sample S6 as a function of wavelength for orders 0 through −3 (continued from Fig. 10 for longer wavelengths). Circles are measured data, and solid lines are predictions from the coherent model. Dashed lines connect data points for a given diffraction order and serve as guides for the eye. Vertical bars show range of predicted efficiencies taking uncertainties in SEM-derived parameters into account.

minimize potential bending and buckling of the grating bars the span between support mesh bars should be shortened to ~10 μm or less [16]. At this point we are not trying to quantify or model the effects of imperfections in further detail, since our fabrication development is leading us to a much improved support mesh geometry with a strongly reduced footprint.

We are presently working on an anisotropic dry etch that is independent of the Si crystal structure and that allows us to etch both CAT grating and support mesh bars close to vertically with high etch anisotropy. We have recently demonstrated such a process to an etch depth of 6 μm [25]. However, due to the resulting larger sidewall roughness, a very short "polishing" step in KOH is still required at the end [16]. Our goal is the fabrication of a highly efficient CAT grating where the integrated support mesh bars occupy no more than 10% of the grating area and feature a cross section that is close to rectangular. A much shorter KOH etch might give rise to smaller duty cycle variations, and the smaller support mesh periods made possible by the dry etch will lead to a stiffer structure with fewer structural defects and improved homogeneity. Figure 12 shows an example theoretical prediction of the absolute diffraction efficiency for such a structure.

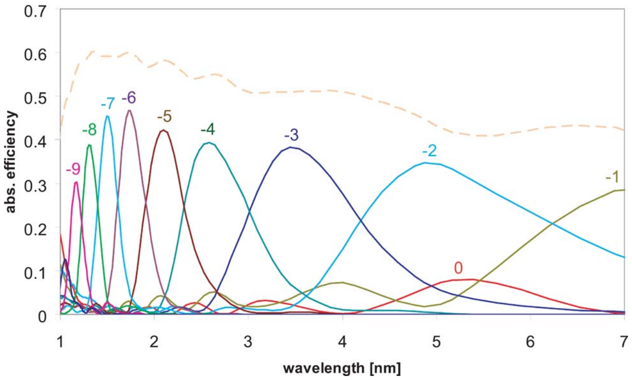

Fig. 12. (Color online) Predicted absolute diffraction efficiencies (solid lines, orders 0 through −10) according to the incoherent model for a CAT grating with a 1D support mesh and the following parameters: $p = 200\,\text{nm}$, $\alpha = 1.5°$, $d = 6186\,\text{nm}$, $p_{\text{SM1}} = 5\,\mu\text{m}$, $s = 100\,\text{nm}$, $g = 4.5\,\mu\text{m}$, and $\langle \text{d.c.} \rangle = 0.19$. The dashed line shows the sum of diffraction efficiencies for orders −1 through −10.

7. Summary

We have presented the first diffraction efficiency measurements for CAT gratings with 200 nm period. The data were analyzed using a RCWA-based model for CAT grating dispersion combined with a scalar model for diffraction from the trapezoidal support mesh. Blazing from the CAT gratings was found at essentially 100% of theoretically predicted performance for $\lambda > 3.5$ and 5.0 nm for samples S4 and S6, respectively. Towards shorter wavelengths we find blazing to gradually become less than predicted by up to a factor of 2. Improvements in fabrication are underway that are expected to lead to CAT gratings with less than 10% support mesh area. Based on our results from this study we can therefore expect individual blazed diffraction orders with greater than 50% absolute efficiency over a broad soft x-ray or extreme ultraviolet band.

We gratefully acknowledge technical support from R. C. Fleming (Space Nanotechnology Laboratory), as well as facilities support from the Space Nanotechnology Laboratory, the Nanostructures Laboratory, and the Microsystems Technology Laboratories (all at MIT). This work was supported by National Aeronautics and Space Administration grants NNX07AG98G and NNX08AI62G. The Advanced Light Source at Lawrence Berkeley National Laboratory is supported by the Director, Office of Science, Office of Basic Energy Sciences, Materials Sciences Division, of the U.S. Department of Energy under contract DE-AC02-05CH11231.

References and Notes

1. Lord Rayleigh, "On the manufacture and theory of diffraction gratings," Philos. Mag., Series 4, **47**, 193–205 (1874).
2. R. Wood, "The echelette grating for the infra-red," Philos. Mag., Series 6, **20**, 770–778 (1910).
3. C.-H. Chang, R. K. Heilmann, R. C. Fleming, J. Carter, E. Murphy, M. L. Schattenburg, T. C. Bailey, J. G. Ekerdt, R. D. Frankel, and R. Voisin, "Fabrication of saw-tooth diffraction gratings using nanoimprint lithography," J. Vac. Sci. Technol. B **21**, 2755–2759 (2003).
4. C.-H. Chang, J. C. Montoya, M. Akilian, A. Lapsa, R. K. Heilmann, M. L. Schattenburg, M. Li, K. A. Flanagan, A. P. Rasmussen, J. F. Seely, J. M. Laming, B. Kjornrattanawanich, and L. I. Goray, "High fidelity blazed grating replication using nanoimprint lithography," J. Vac. Sci. Technol. B **22**, 3260–3264 (2004).
5. A. Rasmussen, A. Aquila, J. Bookbinder, C.-H. Chang, E. Gullikson, R. K. Heilmann, S. M. Kahn, F. Paerels, and M. L. Schattenburg, "Grating arrays for high-throughput soft x-ray spectrometers," Proc. SPIE **5168**, 248 (2004).
6. J. F. Seely, L. I. Goray, B. Kjornrattanawanich, J. M. Laming, G. E. Holland, K. A. Flanagan, R. K. Heilmann, C.-H. Chang, M. L. Schattenburg, and A. P. Rasmussen, "Efficiency of a

grazing-incidence off-plane grating in the soft-x-ray region," Appl. Opt. **45**, 1680–1687 (2006).

7. D. L. Voronov, M. Ahn, E. H. Anderson, R. Cambie, C.-H. Chang, E. M. Gullikson, R. K. Heilmann, F. Salmassi, M. L. Schattenburg, T. Warwick, V. V. Yashchuk, L. Zipp, and H. A. Padmore, "High efficiency 5000 lines/mm multilayer-coated blazed grating for extreme ultraviolet wavelengths," Opt. Lett. **35**, 2615–2617 (2010).
8. C. R. Canizares, J. E. Davis, D. Dewey, K. A. Flanagan, E. B. Galton, D. P. Huenemoerder, K. Ishibashi, T. H. Markert, H. L. Marshall, M. McGuirk, M. L. Schattenburg, N. S. Schulz, H. I. Smith, and M. Wise, "The Chandra high-energy transmission grating: design, fabrication, ground calibration, and 5 years in flight," Publ. Astron. Soc. Pac. **117**, 1144–1171 (2005).
9. R. K. Heilmann, M. Ahn, E. M. Gullikson, and M. L. Schattenburg, "Blazed high-efficiency x-ray diffraction via transmission through arrays of nanometer-scale mirrors," Opt. Express **16**, 8658–8669 (2008).
10. See for example http://ixo.gsfc.nasa.gov/.
11. K. Flanagan, M. Ahn, J. Davis, R. K. Heilmann, D. Huenemoerder, A. Levine, H. Marshall, G. Prigozhin, A. Rasmussen, G. Ricker, M. L. Schattenburg, N. Schulz, and Y. Zhao, "Spectrometer concept and design for x-ray astronomy using a blazed transmission grating," Proc. SPIE **6688**, 66880Y (2007).
12. R. K. Heilmann, M. Ahn, and M. L. Schattenburg, "Fabrication and performance of blazed transmission gratings for x-ray astronomy," Proc. SPIE **7011**, 701106 (2008).
13. R. K. Heilmann, M. Ahn, M. W. Bautz, R. Foster, D. P. Huenemoerder, H. L. Marshall, P. Mukherjee, M. L. Schattenburg, N. S. Schulz, and M. Smith, "Development of a critical-angle transmission grating spectrometer for the International X-Ray Observatory," Proc. SPIE **7437**, 74370G (2009).
14. R. K. Heilmann, J. E. Davis, D. Dewey, M. W. Bautz, R. Foster, A. Bruccoleri, P. Mukherjee, D. Robinson, D. P. Huenemoerder, H. L. Marshall, M. L. Schattenburg, N. S. Schulz, L. J. Guo, A. F. Kaplan, and R. B. Schweikart, "Critical-angle transmission grating spectrometer for high-resolution soft x-ray spectroscopy on the International X-Ray Observatory," Proc. SPIE **7732**, 77321J (2010).
15. M. Ahn, R. K. Heilmann, and M. L. Schattenburg, "Fabrication of 200 nm-period blazed transmission gratings on silicon-on-insulator wafers," J. Vac. Sci. Technol. B **26**, 2179–2182 (2008).
16. M. Ahn, "Fabrication of critical-angle transmission gratings for high efficiency x-ray spectroscopy," Ph.D. thesis (Department of Mechanical Engineering, Massachusetts Institute of Technology, 2009).
17. R. K. Heilmann, C. G. Chen, P. T. Konkola, and M. L. Schattenburg, "Dimensional metrology for nanometer-scale science and engineering: towards sub-nanometer accurate encoders," Nanotechnology **15**, S504–S511 (2004).
18. C. G. Chen, P. T. Konkola, R. K. Heilmann, G. S. Pati, and M. L. Schattenburg, "Image metrology and system controls for scanning beam interference lithography," J. Vac. Sci. Technol. B **19**, 2335–2341 (2001).
19. M. Ahn, R. K. Heilmann, and M. L. Schattenburg, "Fabrication of ultrahigh aspect ratio freestanding gratings on silicon-on-insulator wafers," J. Vac. Sci. Technol. B **25**, 2593–2597 (2007).
20. M. Born and E. Wolf, *Principles of Optics* (Cambridge University Press, 1998).
21. The term a/p in Eq. (4) of Ref. [9] and Eq. (2) of Ref. [12] should have been replaced with $(a/p)^2$.
22. M. G. Moharam, D. A. Pommet, E. B. Grann, and T. K. Gaylord, "Stable implementation of the rigorous coupled-wave analysis for surface-relief gratings—enhanced transmittance matrix approach," J. Opt. Soc. Am. A **12**, 1077–1086 (1995).
23. B. L. Henke, E. M. Gullikson, and J. C. Davis, "X-ray interactions—photoabsorption, scattering, transmission, and reflection at $E = 50$–$30,000$ eV, $Z = 1$–92," At. Data Nucl. Data Tables **54**, 181–342 (1993).
24. See for example J. E. Davis, H. L. Marshall, D. Dewey, and M. L. Schattenburg, "Analysis and modeling of anomalous scattering in the AXAF HETGS," Proc. SPIE **3444**, 76 (1998).
25. P. Mukherjee, A. Bruccoleri, R. K. Heilmann, M. L. Schattenburg, A. F. Kaplan, and L. J. Guo, "Plasma etch fabrication of 60∶1 aspect ratio silicon nanogratings on 200 nm pitch," J. Vac. Sci. Technol. B **28**, C6P70 (2010).